

Adjusting the Anisotropy of 1D Sb₂Se₃ Nanostructures for Highly Efficient Photoelectrochemical Water Splitting

Wooseok Yang, Jihoon Ahn, Yunjung Oh, Jeiwan Tan, Hyungsoo Lee, Jaemin Park, Hyeok-Chan Kwon, Juran Kim, William Jo, Joosun Kim, and Jooho Moon*

Sb₂Se₃ has recently spurred great interest as a promising light-absorbing material for solar energy conversion. Sb₂Se₃ consists of 1D covalently linked nanoribbons stacked via van der Waals forces and its properties strongly depend on the crystallographic orientation. However, strategies for adjusting the anisotropy of 1D Sb₂Se₃ nanostructures are rarely investigated. Here, a novel approach is presented to fabricate 1D Sb₂Se₃ nanostructure arrays with different aspect ratios on conductive substrates by simply spin-coating Sb-Se solutions with different molar ratios of thioglycolic acid and ethanolamine. A relatively small proportion of thioglycolic acid induces the growth of short Sb₂Se₃ nanorod arrays with preferred orientation, leading to fast carrier transport and enhanced photocurrent. After the deposition of TiO₂ and Pt, an appropriately oriented Sb₂Se₃ nanostructure array exhibits a significantly enhanced photoelectrochemical performance; the photocurrent reaches 12.5 mA cm⁻² at 0 V versus reversible hydrogen electrode under air mass 1.5 global illumination.

1. Introduction

Inspired by natural photosynthesis, storing solar energy in the form of chemical fuels via artificial photosynthesis is one of the most promising ways to realize sustainable energy. Among the available chemical fuels, hydrogen produced from water is attractive because of the ubiquitous availability of water and its low-carbon footprint.^[1] Solar hydrogen production can be accomplished by a photoelectrochemical (PEC) system, which simultaneously functions as a light harvester and electrolyzer


in a single device.^[2] Semiconductor materials in a PEC device transform absorbed photons into excited electronic states that drive the electrochemical reaction at the semiconductor–electrolyte interface. To date, numerous semiconductors have been reported as photoelectrodes for PEC water splitting, including Si,^[3,4] III–V group elements,^[5,6] metal oxides,^[7,8] Cu-chalcogenides,^[9,10] and polymers.^[11] However, until now, a nontoxic and low-cost material that can be obtained with scalable processing is not available and therefore, there is ongoing intensive research for exploring new absorber materials.

Antimony triselenide (Sb₂Se₃), composed of comparatively abundant and low-toxic constituents, is an attractive p-type semiconductor for PEC hydrogen production owing to its narrow band gap of 1.0–1.3 eV, high absorption coefficient (>10⁵ cm⁻¹), and high hole mobility.^[12] Moreover, Sb₂Se₃ is a simple binary compound with uniquely a thermodynamically stable orthorhombic phase, which allows avoiding the complexities associated with phase- and defect-control, as encountered in other p-type semiconductors such as Cu(In,Ga)(S,Se)₂ and Cu₂ZnSn(S,Se)₄. With its promising properties, Sb₂Se₃ has been applied in diverse optoelectronic and energy conversion devices such as solar cells,^[13] thermoelectric devices,^[14] photo-detectors,^[15] PEC cells,^[16] and lithium/sodium ion batteries.^[17] Recently, efficient photocathodes for PEC water splitting based on Sb₂Se₃ have been reported.^[18,19] Our group also reported a novel method to fabricate Sb₂Se₃ nanoneedle arrays, to serve as a photocathode for PEC water splitting, by facile spin-coating of a precursor solution without any complicated processes.^[20] Despite the unique growth behavior of the Sb₂Se₃ nanostructures, the growth mechanism and the chemistry of the Sb-Se precursor solution has not yet been elucidated. To establish a reliable strategy to control the Sb₂Se₃ nanostructures, understanding the molecular structure of the involved precursor species and their interactions in the solvent is imperative.

Controlling the shapes of semiconductor nanomaterials has been of great interest because their optical and electrical properties are significantly influenced by the structures of their constituent materials.^[21] In particular, Sb₂Se₃ consists of accumulated [Sb₄Se₆]_n nanoribbons stacked through van der Waals forces along the [100] and [010] axes, whereas strong covalent bonds exist along the [001] axis, resulting in a preferred anisotropic

W. Yang, Dr. J. Ahn, Y. Oh, J. Tan, H. Lee, J. Park, H.-C. Kwon, Prof. J. Moon
Department of Materials Science and Engineering
Yonsei University
50 Yonsei-ro, Seodaemun-gu, Seoul 03722, Republic of Korea
E-mail: jmoon@yonsei.ac.kr

J. Kim, Prof. W. Jo
Department of Physics
Ewha Womans University
Ewhayodae-gil 50, Seodaemun-gu, Seoul 03760, Republic of Korea
Dr. J. Kim
High-Temperature Energy Materials Research Center
Korea Institute of Science and Technology
Seoul 02792, Republic of Korea

 The ORCID identification number(s) for the author(s) of this article can be found under <https://doi.org/10.1002/aenm.201702888>.

DOI: 10.1002/aenm.201702888

growth of Sb_2Se_3 .^[12] This anisotropy leads to anisotropic carrier mobility depending on the transport direction, with the hole mobilities in a single grain along the [100], [010], and [001] directions being 1.17, 0.69, and $2.59 \text{ cm}^2 \text{ V}^{-1} \text{ s}^{-2}$, respectively.^[22] Thus, the efficiencies of thermally evaporated Sb_2Se_3 thin films solar cells are reportedly strongly dependent on their crystallographic orientation.^[23,24] Although some studies on synthesis of Sb_2Se_3 nanowires have been reported;^[25,26] however, the influence of varying the 1D Sb_2Se_3 nanostructure on the photoelectrode performance is rarely investigated.

Here, we demonstrate a novel molecular solution approach for implementing the Sb_2Se_3 nanostructure arrays as photocathodes for PEC water splitting. Shape-controlled Sb_2Se_3 nanostructures were obtained by simply adjusting the solvent ratio of thioglycolic acid (TGA) and ethanolamine (EA). A mixture of thiol-amine, the so-called “alkahest,” is known to be a strong solvent system capable of dissolving diverse compounds, including metals, oxides, and chalcogenides.^[27] High-quality metal chalcogenide thin films could be obtained by a recovering process involving a sequence of dissolving a precursor powder, followed by coating the solution and annealing. Although numerous chalcogenide thin films such as CdS, CuInS₂, CuZnSnS₄, SnS, and V₂VI₃ have been prepared,^[28–30] nanostructuring strategies through the thiol-amine system have been elusive. For the first time, we elucidate the role of the carboxylate nucleophile in dissolving the chalcogen materials, whereas studies on the previously developed alkahest solution-derived chalcogenide materials focused on the role of the thiolate nucleophile. The chemistry of the Sb-Se precursor solution is elucidated by liquid Raman spectroscopy, and the possible growth mechanism is proposed. Deposition of TiO₂ and Pt on the shape-controlled Sb_2Se_3 nanostructures enabled us to demonstrate a remarkable device performance, reaching a photocurrent of 12.5 mA cm^{-2} at 0 V versus reversible hydrogen electrode under air mass 1.5 global (AM 1.5 G) illumination.

2. Results

2.1. Preparation and Analysis of Sb-Se Precursor Solution

Identification of the growth mechanism of solution-derived 1D nanostructures requires an in-depth understanding of the molecular species present in the precursor solution. Because we utilized a solvent mixture of TGA and EA to prepare the Sb-Se precursor solution, investigating the chemical reaction between TGA and EA is a prerequisite for the analysis of the Sb-Se precursor solution. We first analyzed molecular structures of various solvents and subsequently characterized the Sb-Se precursor solution by liquid Raman analysis. This technique offers the unique opportunity to simultaneously prove the vibrational modes of various solvated species. **Figure 1** shows the Raman spectra of TGA, EA, and their mixtures in the molar ratios of 40:60 and 60:40. The peaks attributed to S–C stretching of TGA ($\approx 584 \text{ cm}^{-1}$ for S–C/C–C complex stretching, $\approx 679 \text{ cm}^{-1}$ for S–C gauche conformer, $\approx 763 \text{ cm}^{-1}$ for S–C trans conformer)^[31] are considerably shifted to higher wavenumbers upon mixing with EA (Figure 1a). The shift of the S–C stretching in TGA

toward the positive direction likely results from reduced electron density on the sulfur atom owing to the deprotonation of the carboxylic acid group.^[32] Simultaneously, the peak intensities of C–COOH stretching ($\approx 907 \text{ cm}^{-1}$) and C=O stretching ($\approx 1725 \text{ cm}^{-1}$) decrease, whereas that of C–COO[−] ($\approx 930 \text{ cm}^{-1}$) increases with increasing mixing ratio of EA (Figure 1b,c), indicating that the carbonyl group (C=O) disappears as the carboxylate anion is produced.^[33] When the molar ratio of TGA:EA is 40:60, the peaks of C–COOH and C=O stretching eventually disappear with the concomitant appearance of the NH₂ stretching band at $3100\text{--}3500 \text{ cm}^{-1}$ (Figure 1b–d). In addition, the S–H stretching band at 2573 cm^{-1} diminishes in intensity with increasing ratio of EA, simply due to the reduced proportion of TGA, and rather not owing to the intersolvent interaction, because significant amount of the thiol group (S–H) still remained in TGA:EA = 40:60 (Figure 1e). Our liquid Raman analysis clearly shows that by mixing TGA and EA, amine deprotonates the carboxylic acid (Figure 1f), releasing the carboxylate anions (C–COO[−]), without producing thiolate (C–S[−]) that has been commonly observed in other thiol-amine systems.^[34] Although the use of TGA/EA has been already reported as a solvent for preparing chalcogenide thin films,^[35,36] deprotonation of the carboxylic acid group in a mixture of TGA and EA is confirmed for the first time. This is in accordance with lower $\text{p}K_a$ of the carboxylic acid group (3.83) than that of the thiol group (9.3) in TGA, indicating that the deprotonation of the carboxylic acid is preferred over that of the thiol. The formed carboxylate anion is expected to play a unique role in the preparation of the chalcogen precursor solution in TGA/EA mixture, which is clearly different from the previously reported thiolate-mediated dissolution of the chalcogenide species because the carboxylate anion is a much weaker nucleophile than the thiolate anion.

After analyzing the molecular structures of the TGA-EA mixture solvent, we prepared three different Sb-Se precursor solutions. Three different Se solutions were prepared by adding Se powders into TGA/EA mixtures of varying molar ratios (TGA:EA = 5:95, 20:80, and 40:60). The Sb solutions were prepared by dissolving SbCl₃ in 2-methoxyethanol (2ME). Note that except for the TGA:EA molar ratio, all other parameters including the concentration of Sb and Se were fixed. Three different Sb-Se precursor solutions were obtained by mixing the individual Sb and Se solutions, which are referred hereafter as TGA 5, TGA 20, and TGA 40 Sb-Se solutions, respectively. Detailed experimental methods are described in the Experimental Section. The solvent mixture of TGA 40 provides a higher intensity of the C–COO[−] stretching band compared to those of TGA 5 and TGA 20, indicating an abundance of the carboxylate anions in it (Figure 2a–c). Upon the dissolution of Se powder, the C–COO[−] stretching peak diminished whereas the S–H stretching band changed negligibly (Figure S1, Supporting Information), implying that the carboxylate anion induced the dissolution of Se. Note that the selenium powder is insoluble in a mixed solvent without NH₂ group, i.e., the molar ratio of 60:40 as shown in Figure S2 in the Supporting Information, because the reduction of Se to Se^{2−} to form polyselenide molecules is an amine-catalyzed reaction.^[37] Thus, it is reasonable to assume that selenium dissolution is caused by the cooperative reaction between the carboxylate ion and the

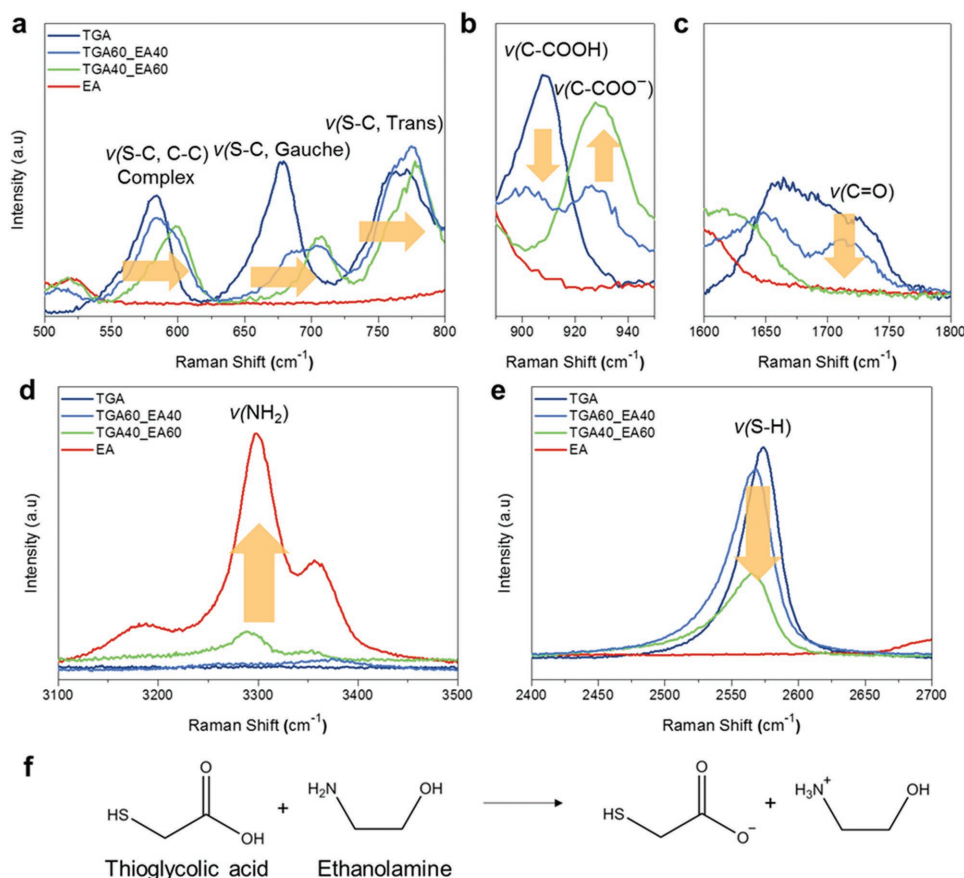


Figure 1. Molecular structure analysis of TGA-EA mixtures. Raman spectra showing a) S–C stretching, b) C–COOH and C–COO[−] stretching, c) C=O stretching, d) NH₂ stretching, and e) S–H stretching. f) The chemical reaction between TGA and EA, showing that the amine deprotonates the carboxylic acid group in TGA, producing the carboxylate nucleophile.

amine group, in our solvent system. In contrast, in a bidentate thiol and amine-based alkalest system such as ethanedithiol/ethylenediamine, the amine deprotonates the thiol group to produce nucleophilic thiolates. The S–H stretching peak has been shown to disappear upon the addition of Se powder, indicating that the chalcogen species dissolves via the formation of Se–S species generated by the nucleophilic thiolates.^[34] After mixing the Se and Sb solutions, a further decrease in the C–COO[−] stretching peak was observed, suggesting that the carboxylate anion was involved in the Sb–Se complex formation (Figure 2b,c).

Figure 2d shows the Raman spectra of the Sb–Se precursor solutions with three different mixing ratios of TGA and EA, as well as SbCl₃ in 2ME and Se solution. Each solution reveals different colors (inset of Figure 2d), indicating that different crystal field effects are produced owing to the unique coordination chemistry between Sb and Se in each solution. Selenium dissolved in TGA/EA to form Se₈ rings and Se chains (i.e., TGA 20 Se solution), analogous to previously reported Se dissolution in water with the aid of diethylenetriamine and hydrazine.^[37,38] Interestingly, upon the addition of the Sb solution into Se solution (i.e., TGA 20 Sb–Se solutions), the peak corresponding to the Se chain ($\approx 247 \text{ cm}^{-1}$) disappears, whereas the peak of the Se₈ ring ($\approx 264 \text{ cm}^{-1}$) remains the same. The

peaks of Sb ions (≈ 300 and $\approx 347 \text{ cm}^{-1}$) observed for the Sb solution (i.e., Sb³⁺ in 2ME) also disappear, while a new peak at 212 cm^{-1} (as indicated by the red arrow) is apparent. The disappearance of the Se chain peaks was observed regardless of the TGA/EA molar ratio (Figure S3, Supporting Information). This new peak may be assigned to the Sb–Se chain formation because its appearance is closely related to the disappearance of both the peaks of Se chains and Sb ions. Previous Raman analysis of hydrazine-based Sb–Se solutions also attributed this Sb–Se peak to [Sb₄Se₇]^{2−}, which has a structure similar to that of the 1D Sb₄Se₆ ribbon.^[39] Thus, we can reasonably assign the peak at 212 cm^{-1} to [Sb₄Se₇]^{2−}. TGA 40 Sb–Se solution exhibits a sharp [Sb₄Se₇]^{2−} chain peak, whereas shoulder peaks (indicated by the blue arrow) appear with decreasing ratio of TGA with respect to EA. A plausible explanation for these shoulder peaks is that relatively short [Sb₄Se₇]^{2−} chains are likely to exist in TGA 5 Sb–Se and TGA 20 Sb–Se precursor solutions, whereas long Sb–Se chains prevail in TGA 40 Sb–Se precursor solution. Because the edge state of the [Sb₄Se₇]^{2−} chain reveals a slightly different vibration mode, a larger amount of the edge states associated with short [Sb₄Se₇]^{2−} chains in TGA 5 Sb–Se solution likely manifest as higher intensity shoulder peaks, as similarly observed in finite-size graphite and graphene edges.^[40] Considering that the dissolved chalcogenide species in the alkalest

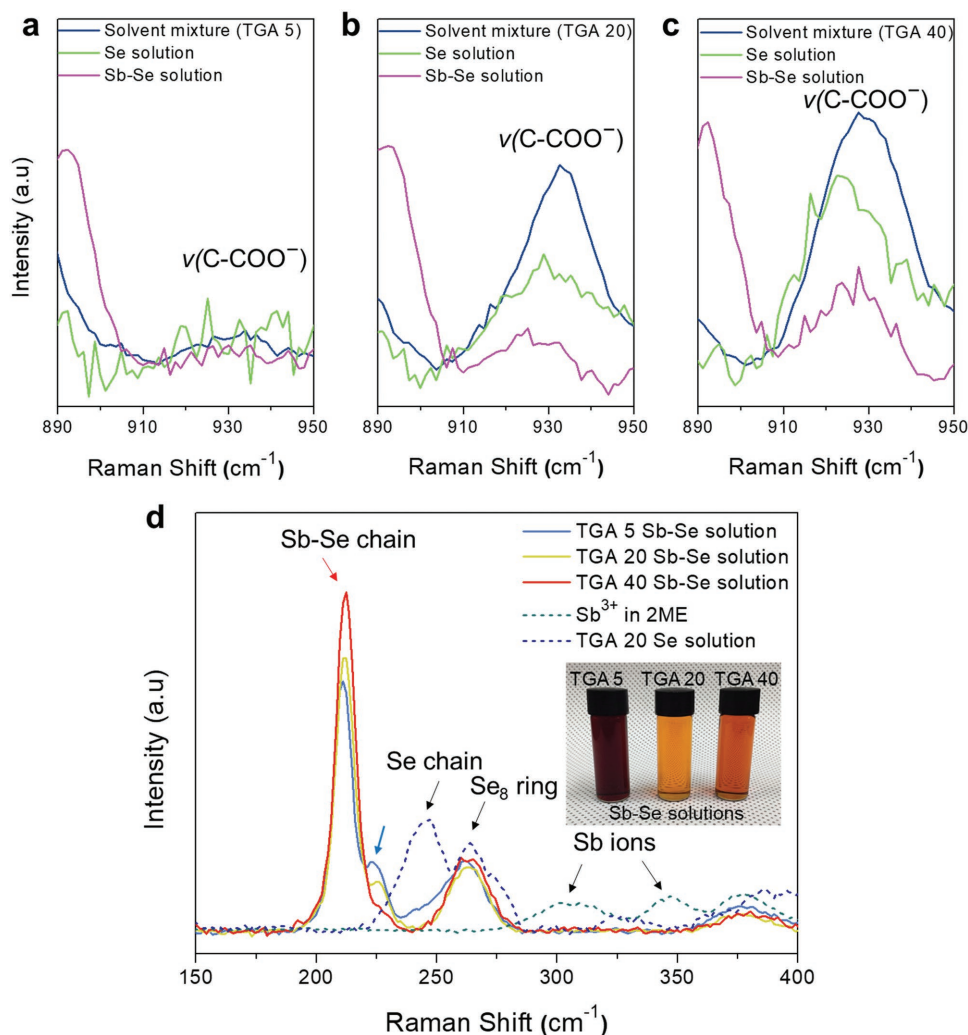


Figure 2. Molecular structure analysis of Sb-Se precursor solution as well as Sb and Se solutions. a–c) Raman spectra showing carboxylate stretching in TGA 5, TGA 20, and TGA 40 Sb-Se precursor solutions. d) Raman spectra of the Sb-Se chain with Se chain, Se₈ ring, and Sb ions. After mixing the Sb solution with Se solution (dashed lines), peaks corresponding to both the Sb ions and Se chain disappear, whereas the peak due to the Se₈ ring remains the same. The blue arrow represents the shoulder peaks.

solvent exist in the form of amine-ligated chalcogenometallate anions counterbalanced by NH₃⁺,^[27] the negatively charged Sb-Se chain are envisaged to be counterbalanced by the NH₃⁺ moiety produced by the protonation of the amine group.

2.2. Fabrication of Sb₂Se₃ Nanostructure Arrays

For the three different Sb-Se precursor solutions, the morphological evolution of the Sb₂Se₃ nanostructures as a function of the spin-coating iteration number was examined (Figure 3). After the first spin-coating, TGA 40 Sb₂Se₃ already exhibits 1D needle-like structures, whereas no specific 1D morphology is observed in TGA 5 Sb₂Se₃. As the number of spin-coating iterations increases, the length of TGA 40 Sb₂Se₃ considerably increases, while the diameter changes negligibly. In contrast, the nanostructures of TGA 5 Sb₂Se₃ indicate a relatively enlarged diameter with a nearly invariant length. The statistics

obtained by analyzing 20 nanostructures corresponding to different TGA: EA ratios are displayed in Figure S4 in the Supporting Information. The individual 1D Sb₂Se₃ nanostructures with different solvent mixture ratio were analyzed in detail by transmission electron microscopy, as shown in Figure S5 in the Supporting Information. With increasing proportion of TGA, 1D Sb₂Se₃ becomes elongated, in accordance with the scanning electron microscopy (SEM) observations. Despite the difference in the aspect ratio, all TGA-derived Sb₂Se₃ nanostructures have the same crystallographic orientation regardless of the observation point, i.e., needle-like growth with their length along the [001] direction, similar to those observed in previous studies.^[20,41–44] In addition, all Sb₂Se₃ nanostructures reveal uniform compositional distributions with a stoichiometric Se/Sb value of 1.5 (Figure S6, Supporting Information). Regardless of the TGA ratio, the synthesized Sb₂Se₃ nanostructures have an identical absorption edge near 1000 nm wavelength and a direct band gap energy (E_g) near 1.25 eV, as obtained by

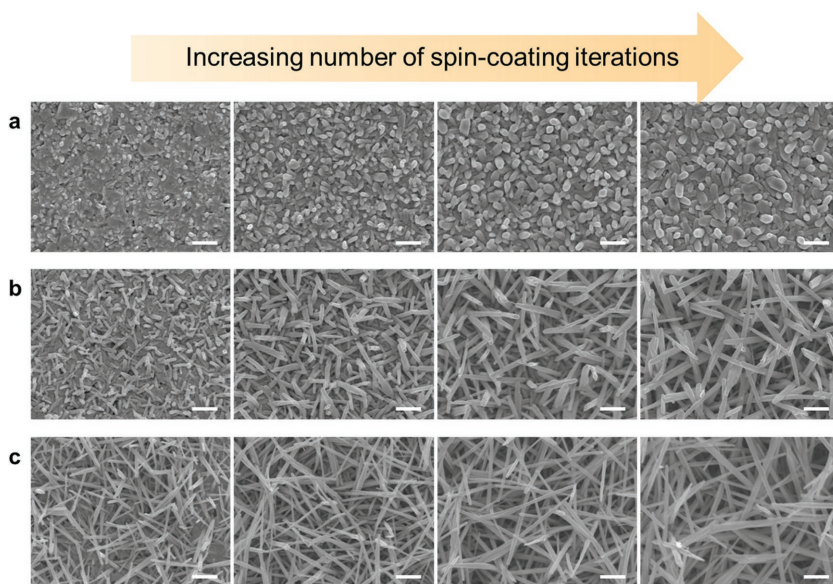


Figure 3. Morphological evolution of the Sb_2Se_3 nanostructures as a function of the number of spin-coating iterations. Top-view SEM images of a) TGA 5, b) TGA 20, and c) TGA 40 Sb_2Se_3 nanostructures after different spin-coating iterations. The images in each column show Sb_2Se_3 after two, four, six, and eight coatings from the left (scale bar = 500 nm).

extrapolating the linear region of the $(\alpha h\nu)^2$ versus $h\nu$ graph, i.e., the Tauc plot (Figure S7, Supporting Information).

All TGA Sb-Se precursor solutions enabled us to produce 1D Sb_2Se_3 nanostructures with identical crystallographic, compositional, and optical characteristics, except for the varied aspect ratios. These morphological features can be attributed to our unique solution system containing carboxylate anions. In a

previous report, ethanedithiol-based thiol-amine system, i.e., without the carboxylate anions, led to the production of an Sb_2Se_3 thin film without any specific 1D nanostructuring.^[28] In addition, simultaneous disappearance of the Se chain and Se_8 ring was reported upon the addition of the metal cations to the chalcogenide molecular solution.^[38] In contrast, Se chains are selectively consumed in our TGA-EA mixtures to form negatively charged $[\text{Sb}_4\text{Se}_7]^{2-}$ chains, while the Raman peak of the carboxylate anions disappear upon the formation of the $[\text{Sb}_4\text{Se}_7]^{2-}$ chains. We propose a plausible mechanism for the morphological variation, as schematically described in **Figure 4**. During the $[\text{Sb}_4\text{Se}_7]^{2-}$ formation process, the carboxylate anions may act as capping agents and adsorb on the Se chains.^[45] Compared to TGA 5 Sb-Se, the abundant carboxylate anions in the TGA 40 Sb-Se solution are capable of hindering the lateral reaction between Sb and Se, allowing the growth of longer $[\text{Sb}_4\text{Se}_7]^{2-}$ chains. Because TGA 40 Sb-Se solution contains longer $[\text{Sb}_4\text{Se}_7]^{2-}$ chains than in other

TGA/EA mixing ratios and the Sb_4Se_6 ribbon is the main constituent of the Sb_2Se_3 crystal in which ribbons are stacked along the [001] direction via strong covalent bonding, TGA 40 Sb_2Se_3 would lead to needle-shaped nanostructures with a longer length than those of TGA 5 and TGA 20 Sb_2Se_3 . Thus, the amount of the carboxylate moiety is a critical factor for controlling the aspect ratio of the 1D Sb_2Se_3 nanostructures.

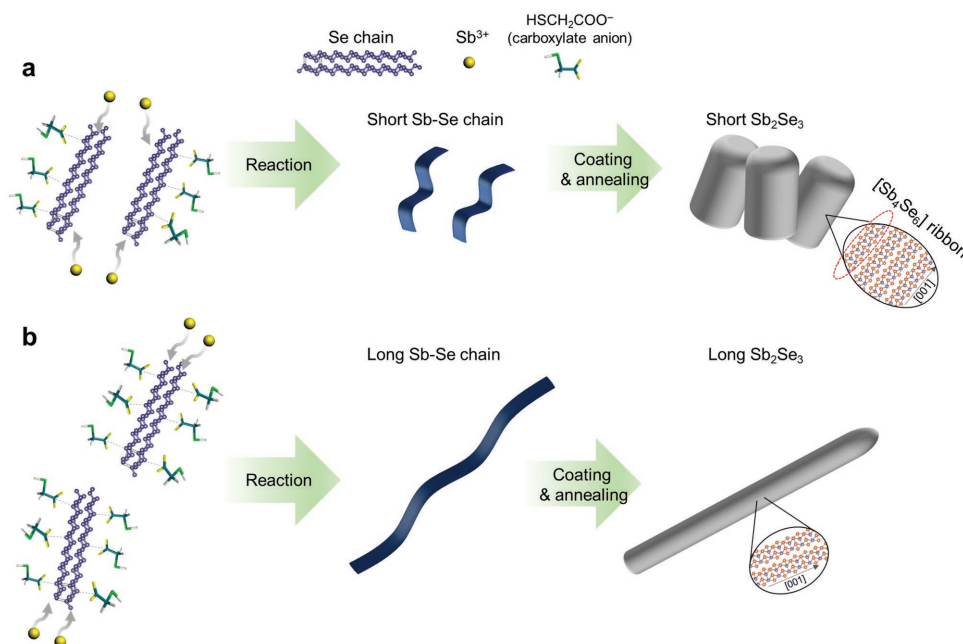


Figure 4. Schematic illustration of the proposed formation mechanism of the Sb_2Se_3 nanostructure. a) A few carboxylate anions partially adsorb on the Se chains and Sb^{3+} react with the Se chains, resulting in the formation of short Sb_2Se_3 nanostructures. b) Abundant carboxylate anions fully adsorb on the Se chain and the lateral growth of Sb_2Se_3 is restricted by these ions, consequently leading to the formation of long Sb_2Se_3 nanostructures (dimensions not to scale).

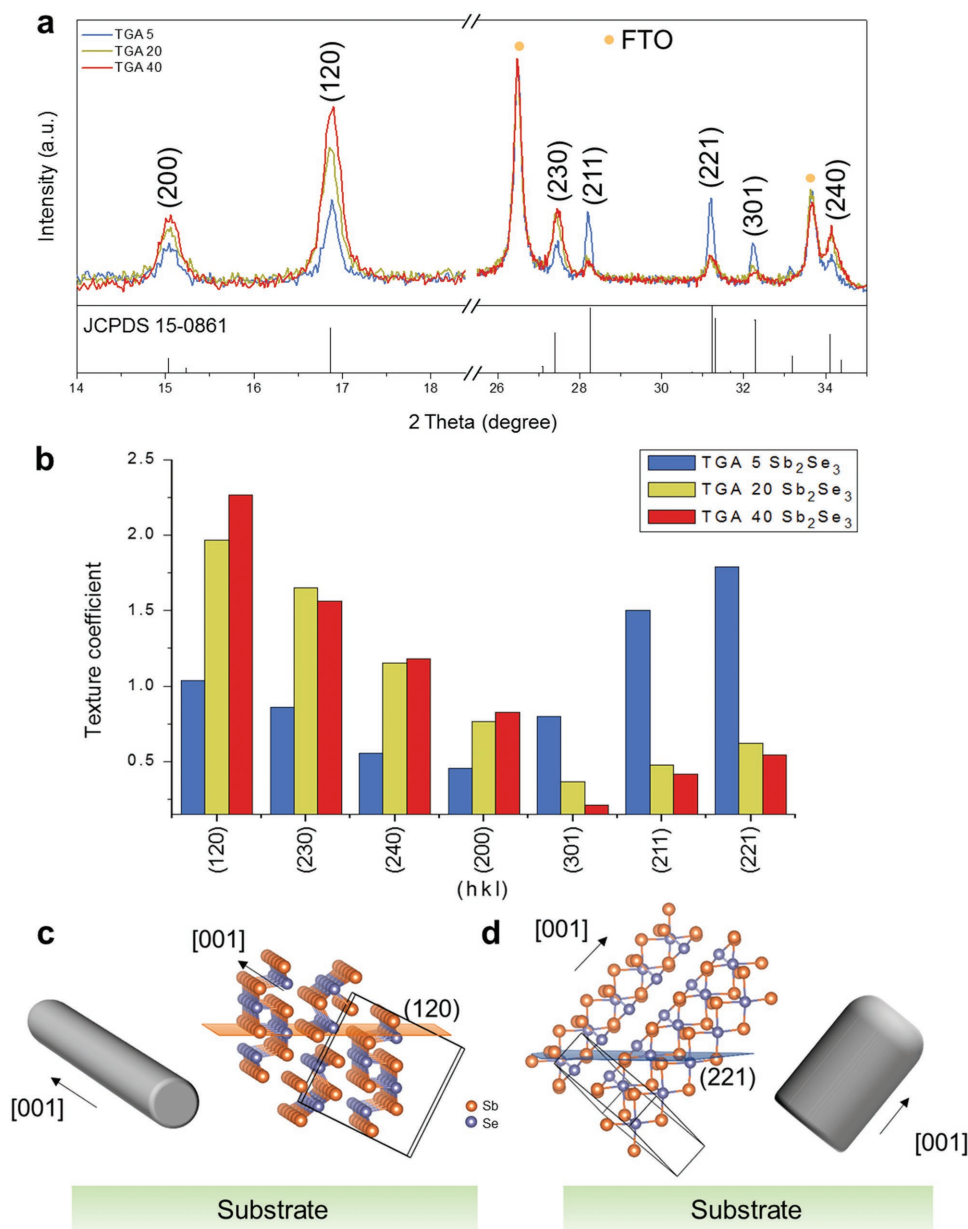


Figure 5. Preferred orientation of the Sb_2Se_3 nanostructure arrays. a) X-ray diffraction patterns of the Sb_2Se_3 nanostructures prepared with different ratios of the solvent mixture. b) The texture coefficients of selected diffraction peaks in different Sb_2Se_3 nanostructure arrays. c,d) Schematic showing the orientation and atomic structures of long and short Sb_2Se_3 nanostructures.

Figure 5a shows the X-ray diffraction (XRD) patterns of the Sb_2Se_3 nanostructures obtained from different TGA Sb-Se solutions on Au/fluorine-doped tin oxide (FTO) substrates. Interestingly, the intensities of the $(hk0)$ planes, which are parallel to the c -axis, are enhanced with increasing proportion of TGA with respect to EA, whereas higher intensities of the (211), (221), and (301) peaks are observed in TGA 5-derived Sb_2Se_3 . To quantify the preferred orientation, we calculated the texture coefficient T_c , which is defined as

$$T_c(hkl) = n \frac{I(hkl)/I_o(hkl)}{\sum_1^n I(hkl)/I_o(hkl)} \quad (1)$$

where $I(hkl)$ is the measured relative intensity of the peak corresponding to the hkl diffraction, $I_o(hkl)$ is the relative intensity from a standard powder sample (Joint Committee on Powder Diffraction Standards, JCPDS No. 15-0861), and n is the total number of diffraction peaks used in the evaluation. A large T_c value for a specific diffraction peak indicates preferred orientation along this direction. In the present case, we chose seven diffraction peaks ($n = 7$) corresponding to 2θ values of 120, 230, 240, 200, 301, 211, and 221. Clearly, for TGA 40 Sb_2Se_3 nanostructures, the T_c values of the $(hk0)$ planes have higher intensities, whereas TGA 5 Sb_2Se_3 array reveals relatively high $T_c(hkl)$ (Figure 5b). Individual Sb_2Se_3 nanostructures have identical crystallographic orientation (Figure S5, Supporting

Information), i.e., their length along the [001] direction, regardless of the nanowire aspect ratio. Accordingly, variation in the alignment of the 1D nanostructure arrays with respect to the substrate is responsible for the preferred orientation observed in the XRD data. As shown in Figure 5c,d, longer nanowires tend to be more inclined to the plane of the substrate, whereas shorter nanorods exist at a relatively higher tilted angle with respect to the substrate. This explanation is in good agreement with the cross-sectional SEM images (Figure S8, Supporting Information). The crystalline orientation strongly affects the efficiency of the Sb_2Se_3 -based devices because the carrier transport in Sb_2Se_3 is considerably influenced by the crystallographic orientation. For example, Zhou et al. reported that the efficiency of the [221]-oriented Sb_2Se_3 thin film solar cell is much higher than that of a [120]-oriented one because carriers travel within the covalently bonded $(\text{Sb}_4\text{Se}_6)_n$ ribbons in the former, whereas they are required to hop between the ribbons held together by van der Waals forces in the latter.^[23] Thus, it is reasonable that the PEC performance of our TGA-derived Sb_2Se_3 photocathodes would also be affected by the TGA/EA solvent ratio.

2.3. Photoelectrochemical Properties of the Sb_2Se_3 Nanostructure Arrays

Figure 6 shows the linear sweep voltammograms (LSV) under intermittent-light illumination (AM 1.5 G) for the Sb_2Se_3 nanostructures after the depositions of n-type TiO_2 and a Pt catalyst. Most of the p-type chalcopyrite photocathodes require n-type overlayer and cocatalyst because PEC performance of the photocathodes is commonly limited by poor charge separation and less catalytic property.^[2] Figure S9 in the Supporting Information shows the SEM images of Sb_2Se_3 nanostructures after surface modification with TiO_2 and Pt. It should be noted that photoelectrochemically deposited Pt nanoparticles are nearly invisible due to their small size (<5 nm). The thickness of all Sb_2Se_3 nanostructures uniformly increases upon deposition of TiO_2 , indicative of conformal deposition of TiO_2 regardless of the aspect ratios. Band alignment among Au, Sb_2Se_3 , and TiO_2 is shown in Figure S10 in the Supporting Information and the roles of TiO_2 and Pt were discussed in detail in our previous study.^[20] All PEC measurements, including linear sweep voltammograms, chronoamperometric (CA) measurements, were performed with the sample area of 0.9 cm^2 in argon-purged 0.1 M aqueous H_2SO_4 (pH ≈ 1) under simulated one-sun illumination (AM 1.5 G, 100 mW cm^{-2}). A remarkable photocurrent of -12.5 mA cm^{-2} at 0 V versus reversible hydrogen electrode (RHE) was obtained for the $\text{Pt}/\text{TiO}_2/\text{Sb}_2\text{Se}_3$ (TGA 5) sample, whereas $\text{Pt}/\text{TiO}_2/\text{Sb}_2\text{Se}_3$ (TGA 40) revealed only -5 mA cm^{-2} at 0 V versus RHE. The onset potential, defined as the potential showing $50 \mu\text{A cm}^{-2}$ of cathodic photocurrent in the I - E curves, is near 0.35 V versus RHE regardless of the samples synthesized from different TGA Sb-Se precursor solutions. Compared to other emerging earth-abundant photocathode materials, as summarized recently by Septina et al., our Sb_2Se_3 nanostructures clearly demonstrate the highest photocurrent reaching 12.5 mA cm^{-2} at 0 V versus RHE, whereas the onset potential needs to be further improved (Table S1, Supporting

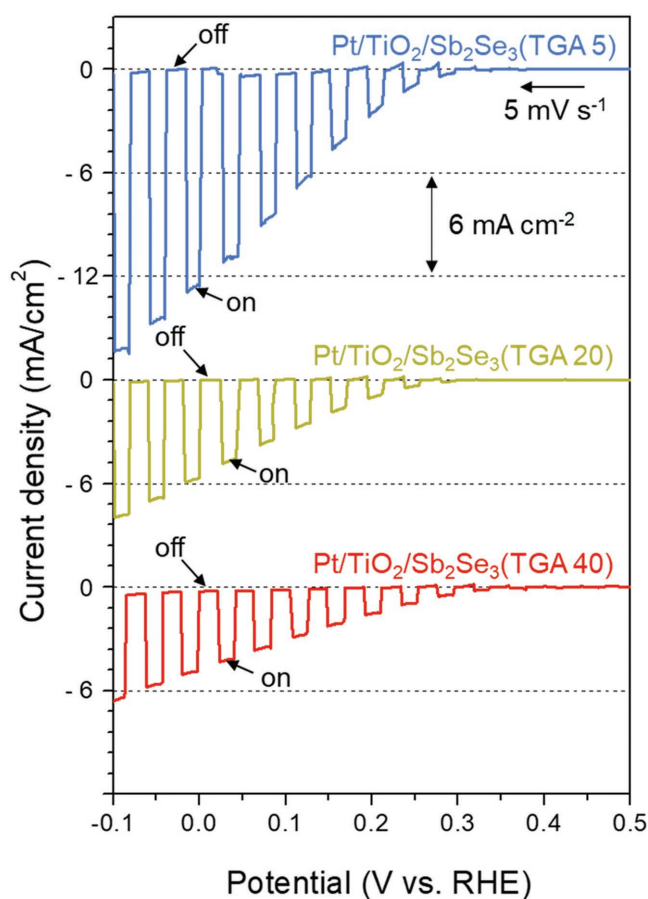


Figure 6. Photoelectrochemical properties. Linear sweep voltammograms under intermittent-light illumination (AM 1.5 G) of $\text{Pt}/\text{TiO}_2/\text{Sb}_2\text{Se}_3$ photocathodes (area: 0.9 cm^2) in a 0.1 M H_2SO_4 electrolyte. Sb_2Se_3 was prepared using different ratios of the solvent mixture. Pt deposition was performed by the PEC method in a solution containing H_2PtCl_6 , by applying a potential of $-0.6 \text{ V}_{\text{Ag}/\text{AgCl}}$ for 10 min.

Information).^[46] The relatively smaller onset potential likely results from the recombination of photoexcited charge carrier at $\text{TiO}_2/\text{Sb}_2\text{Se}_3$ and/or $\text{Sb}_2\text{Se}_3/\text{Au}$ interfaces (Figure S10, Supporting Information) as commonly observed in PEC devices.^[47] Thus, it is expected that proper interfacial engineering such as the implementation of proper hole selective layers^[48] or buffer layers^[49] could enhance the onset potential.

In general, the efficiency of a PEC device is a summation of three efficiency factors: η_{e^-/h^+} , $\eta_{\text{transport}}$, and $\eta_{\text{interface}}$, which refer to the efficiency of the generation of electrons and holes from incoming photons, the efficiency of charge separation through the semiconductor, and the efficiency of charge transfer at the solid-liquid interface, respectively.^[50] Because $\eta_{\text{interface}}$ is strongly determined by the cocatalyst and Pt was implemented as a cocatalyst for all Sb_2Se_3 -based photocathodes, it is reasonable to postulate that $\eta_{\text{interface}}$ for these three Sb_2Se_3 have negligible differences. From the viewpoint of light absorption, TGA 40 Sb_2Se_3 rather absorbs more photons within the range of visible light even though all samples have an identical absorption edge (Figure S7, Supporting

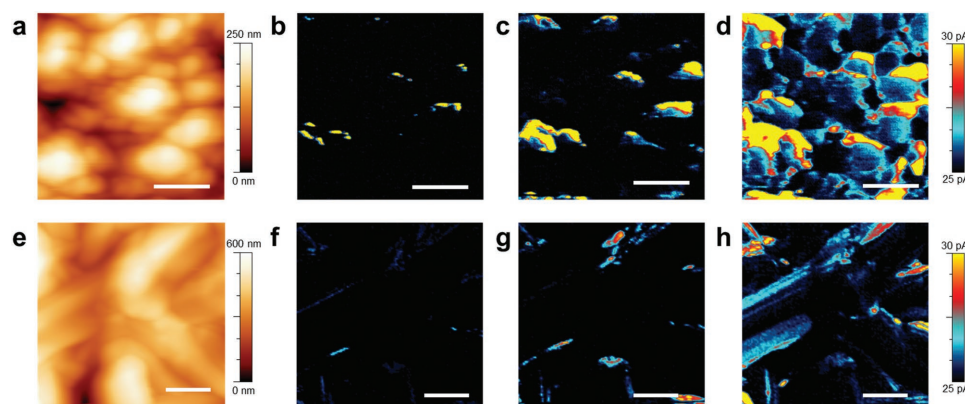


Figure 7. Analysis of the charge transport by conductive atomic force microscopy (c-AFM). a–d) TGA 5 Sb_2Se_3 . a) Topography and current maps at a tip-sample voltage of b) -3 V, c) -6 V, and d) -9 V. e–h) TGA 40 Sb_2Se_3 . (e) Topography and current maps at a tip-sample voltage of (f) -3 V, (g) -6 V, and (h) -9 V (scale bar = 500 nm).

Information). The enhanced absorption of the visible light by TGA 40 Sb_2Se_3 can be attributed to the light scattering due to their hundreds of nanometer-scale nanostructures, whereas TGA 5 Sb_2Se_3 reflects visible light to some extent (Figure S11, Supporting Information). Thus, we can assume that $\eta_{\text{transport}}$ of TGA 5 Sb_2Se_3 nanostructure is much higher than that of TGA 40. To examine the charge carrier transport through the Sb_2Se_3 nanostructure, we performed conductive atomic force microscopy (c-AFM) analysis, which is well known as an efficient technique for investigating charge carrier transport in nanostructured photoelectrode.^[51] Figure 7a,e shows the topographic images of TGA 5 and TGA 40 Sb_2Se_3 nanostructures. Sb_2Se_3 nanostructures derived from TGA 40 revealed longer 1D structures in accordance with the SEM images in Figure 3. With increasing external bias, the well-distributed high current region was observed without particular 1D direction in TGA 5 Sb_2Se_3 (Figure 7b–d), whereas the current map of TGA 40 Sb_2Se_3 reveals 1D direction with a relatively small current level (Figure 7f–h). The difference in the current distribution can be understood based on the fact that the [221]-oriented TGA 5 Sb_2Se_3 nanostructure array consists of tilted $[\text{Sb}_4\text{Se}_6]_n$ ribbons vertically stacked on the substrate; thus, the electronic carriers are easily collected in a vertical direction through the covalently bonded ribbons. In contrast, because the [120]-oriented TGA 40 Sb_2Se_3 array consists of $[\text{Sb}_4\text{Se}_6]_n$ ribbons nearly horizontally stacked in parallel to the substrate, the electronic carriers should hop between the ribbons held together by van der Waals forces. Owing to the relatively high resistance along the van der Waals direction, the carrier collection in TGA 40 Sb_2Se_3 nanostructures is relatively inefficient, resulting in the recombination of the photogenerated carrier. In particular, the end parts of the nanowires exhibit larger current, implying that TGA 5 Sb_2Se_3 facilitates a better carrier separation and hence, better performance.^[23] The c-AFM data are clearly consistent with the PEC device performance. The carrier behavior in our Sb_2Se_3 photoelectrode is schematically illustrated in Figure S12 in the Supporting Information.

Stable operation of the photocathode is a crucial factor for practical application in a PEC device. Thus, the stability of the Pt/ TiO_2 / Sb_2Se_3 (TGA 5) photocathode was evaluated using CA measurements at 0 V versus RHE. We found that the stability of

our Sb_2Se_3 -based photocathode strongly depends on the Pt deposition condition, implying that the deactivation of the photocathode mainly results from the Pt cocatalyst and is not related to Sb_2Se_3 or TiO_2 . Prabhakar et al. demonstrated that Sb_2Se_3 semiconductor is stable under PEC operation condition by performing 285 cycles of cyclic voltammetry in 1 M H_2SO_4 under one-sun illumination.^[18] Figure S13 in the Supporting Information shows that the XRD spectra of the Sb_2Se_3 photocathodes before and after the CA measurement. The XRD data clearly show negligible change after CA measurement, manifesting that the decreased photocurrent density of Sb_2Se_3 based photocathodes was irrelevant to Sb_2Se_3 or TiO_2 . In addition, with increasing deposition time of Pt, the current density was found to slightly decrease owing to reduced light absorption due to hindrance by the catalyst (Figure S14, Supporting Information). Only about 20% photocurrent was maintained after 20 min for the sample with Pt deposited for 10 min, whereas retention of 55% of the photocurrent was observed after 120 min deposition time of Pt (Figure S14b, Supporting Information). This explanation is further supported by the fact that the photocurrent was recovered by replatinization, i.e., depositing an additional fresh layer of the Pt cocatalyst after 5 h stability test (Figure S15, Supporting Information). The instability of Pt cocatalyst is frequently observed in other photocathode systems.^[11,52,53] Rovelli et al. commented the possibility of Pt deactivation during PEC measurement due to the formation of Pt chalcogenides.^[52] In order to improve the stability resulting from the Pt cocatalyst, the Grätzel group demonstrated that ruthenium oxide shows robust binding with a TiO_2 protection layer as an alternative cocatalyst for hydrogen evolution.^[53] In addition, facile Pt detachment from Pt/ TiO_2 /P3HT:PCBM/[(6,6)-phenyl-C61-butryic acid methyl ester]/CuI/FTO during photocathode operation was reported by Rojas et al. and they implemented a solution-processed polyethyleneimine protective coating to halt cocatalyst detachment.^[11] Thus, we believe further optimization of the cocatalyst will enable stable Sb_2Se_3 -based photocathodes. The amount of evolved H_2 from the Pt/ TiO_2 / Sb_2Se_3 (TGA 5) photocathode was also evaluated. As shown in Figure S16 in the Supporting Information, Pt/ TiO_2 / Sb_2Se_3 (TGA 5) photocathode revealed nearly 100% of Faradaic efficiency, indicating the absence of side reactions.

3. Discussion

There is a dilemma with respect to the requirement of a large band gap material to generate sufficient driving force, yet a small enough band gap material to harvest a broad range of the solar spectrum. In this regard, numerous studies have focused on a tandem PEC system in which multiple absorbers are utilized to realize water splitting with high efficiencies.^[54] The efficiencies of tandem cells strongly depend on the band gap combination of two absorbers, while the implementation of a small band gap semiconductor as a bottom absorber is imperative to capture infrared light of the solar spectrum. For example, Prevot et al. estimated a maximum solar to hydrogen efficiency (η_{STH}) of 21.6% with optimal values of $E_{\text{g}1} = 1.89$ and $E_{\text{g}2} = 1.34$ eV based on the Bolton's method, in two semiconductors connected in series, where, $E_{\text{g}1}$ and $E_{\text{g}2}$ are the band gaps of the top and bottom electrodes, respectively.^[55] Further, the Lewis group reported detailed balance calculations, predicting that the maximum η_{STH} can be achieved by the band gaps of $E_{\text{g}1} = 1.6\text{--}1.8$ eV and $E_{\text{g}2} = 0.95\text{--}1.15$ eV.^[54] However, most of the previously reported light absorbing p-type semiconductors have a band gap higher than 1.5 eV; thus, bottom absorbers capable of harvesting the solar spectrum within the infrared region are elusive.^[2] In this regard, a small band gap of Sb_2Se_3 (in our case, 1.25 eV) can be promising for it to serve as a bottom electrode for PEC tandem devices. According to the Lewis's calculation, the tandem device based on our Sb_2Se_3 in conjunction with a photoanode having $E_{\text{g}} = 1.8$ eV ideally yields maximum η_{STH} of 21.5%. Moreover, it is known that the band gap of our Sb_2Se_3 can be tuned from 1.08 to 1.62 eV by substituting Se with S and the tunability of the band gap offers great flexibility in constructing efficient tandem cells.^[39]

Incident photon-to-current conversion efficiency (IPCE) of our Pt(2h)/ $\text{TiO}_2/\text{Sb}_2\text{Se}_3$ photocathode under monochromatic illumination showed that our Sb_2Se_3 -based photocathode is capable of harvesting the solar spectrum up to 1000 nm (Figure 8). The integrated photocurrent density reached to 8.2 mA cm^{-2} , which was nearly identical to the photocurrent density from LSV measurement in Figure S14 in the

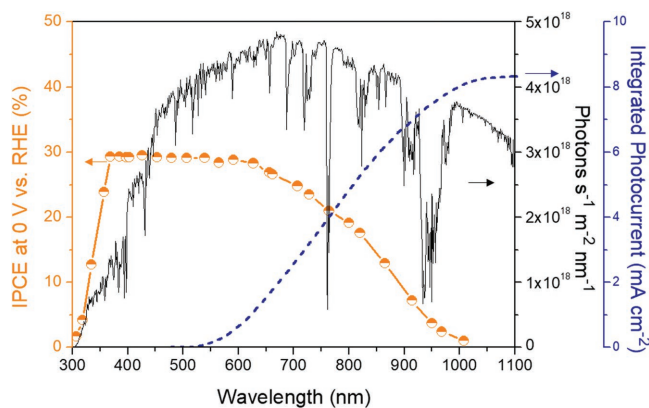


Figure 8. Incident-photon-to-current-efficiency (IPCE) of a Pt(2h)/ $\text{TiO}_2/\text{Sb}_2\text{Se}_3$ (TGA 5) photocathode biased at 0 V versus RHE in $0.1 \text{ M H}_2\text{SO}_4$ electrolyte. Integration of the IPCE values with the solar AM 1.5 spectrum (black line) gives the same photocurrent value (dotted line) as observed with our simulated one-sun illumination.

Supporting Information. This unique infrared harvesting ability of the Sb_2Se_3 photocathode was manifested by the photocurrent estimated by the integration of the IPCE values with the solar AM 1.5 spectrum, reaching saturation near 1000 nm. These IPCE data clearly demonstrated the feasibility of efficient tandem devices based on our Sb_2Se_3 photocathodes as a bottom electrode. However, the insufficient photovoltage of the Sb_2Se_3 photocathode would pose an obstacle for its application in a bias-free tandem device for water splitting. As we mentioned above, the introduction of a proper interface engineering will likely enhance the photovoltage of our Sb_2Se_3 photocathode, as reported by numerous literatures.

4. Conclusions

In summary, we have demonstrated a novel method for adjusting the anisotropy of Sb_2Se_3 nanostructures by modulating Sb-Se precursor solutions at the molecular level. The presence and role of the carboxylate moiety in preparing the Sb-Se solutions were elaborated for the first time by analyzing molecular structures in the solution phase by Raman spectroscopy. The abundant carboxylate anions assisted the formation of long Sb-Se chains at the molecular level and consequently lead to 1D Sb_2Se_3 nanowires with high aspect ratios. By contrast, a relatively small amount of the carboxylate anion in the TGA 5 Sb-Se solution induced a relatively shorter 1D nanorod array of Sb_2Se_3 . After surface modification with TiO_2 and Pt, a remarkable photocurrent 12.5 mA cm^{-2} at 0 V versus RHE was achieved for the TGA 5 Sb_2Se_3 photocathode. The high photocurrent generated in TGA 5 Sb_2Se_3 is explained by appropriately [221]-oriented nanostructure array in which tilted $[\text{Sb}_4\text{Se}_6]_n$ ribbons are vertically stacked on the substrate, so that the electronic carrier could be easily transported to the vertical direction through the covalently bonded ribbons. With the molecular solution-derived Sb_2Se_3 nanostructures, our work highlighted the potential of the Sb_2Se_3 photocathode for hydrogen production through PEC water splitting. Furthermore, the light harvesting capability of the Sb_2Se_3 -based photocathode up to 1000 nm promises the application of Sb_2Se_3 as a bottom electrode for tandem PEC devices, enabling efficient bias-free water splitting.

5. Experimental Section

Preparation of the Sb_2Se_3 Nanostructures: Preparation method for Sb_2Se_3 nanostructures is identical to our previous report,^[20] except for the mixing ratios of TGA and EA. The Sb-Se solutions were prepared by mixing an Sb solution and Se solution. The Sb solution was obtained by dissolving 0.1 M SbCl_3 (99.99%, Alfa Aesar, Heysham, UK) in 12 mL of 2ME (99.5%, Sigma-Aldrich), and the Se solution was obtained by dissolving 0.405 g of the Se powder (99.5%, Sigma-Aldrich, St. Louis, MO, USA) in a mixture of EA (99.5%, Sigma-Aldrich) and TGA (98%, Sigma-Aldrich). The molar ratio of TGA: EA was varied from 5:95 to 40:60 to prepare three different solutions. The Sb-Se solutions were magnetically stirred overnight on an $80 \text{ }^\circ\text{C}$ hot plate inside an N_2 -filled glove box and the resulting solutions were spin coated onto 60 nm thick Au-coated FTO glass (TEC-15, Pilkington, UK). Before coating, the substrate was sonicated in isopropanol for 15 min, followed by UV treatment for 15 min. The spin-coating process was performed at

2000 rpm for 30 s and the as-deposited precursor films were sequentially dried on a preheated hot plate at 180 and 300 °C for 3 min in the N₂-filled glove box. The spin-coating process was repeated two to eight times (Figure 3) to show the growth behavior and six times for other characterization. The as-dried samples were annealed at 350 °C for 20 min in the N₂-filled glove box and postannealed in air at 200 °C for 30 min.

Characterization of the TGA/EA Solutions and Sb₂Se₃ Nanostructures: Raman spectra were recorded on a Horiba Jobin-Yvon LabRAM ARAMIS spectrometer using an Ar-ion laser beam at the excitation wavelength of 514 nm. The morphologies of the Sb₂Se₃ nanostructures were examined using a field emission scanning electron microscope (JSM-6701F, JEOL, Tokyo, Japan) in conjunction with energy dispersive X-ray spectroscopy (EDS) and a transmission electron microscope (Talos F200X, FEI, Hillsboro, OR, USA). Phase analysis of the Sb₂Se₃ nanostructures was performed using XRD (MiniFlex 600, Rigaku, Tokyo, Japan) with Cu K_α radiation ($\lambda = 0.15406$ nm). The optical properties were recorded at room temperature using a UV-vis spectrophotometer (V-670, JASCO, Easton, MD) equipped with an integrating sphere. A Pt/Ir-coated tip (Nanosensor, PPP-EMF: PointProbe® plus electrostatic force microscopy) was used for c-AFM measurements. An external bias voltage was applied from -3 to -9 V. The conducting probe was connected to the ground and the current was detected with a single terminal. To avoid the influence of the morphology on the current signal, the scan rate was lowered to 0.1 Hz and an active trace that measured the topography and the current signal separately was used.

Deposition of TiO₂ on the Sb₂Se₃ Nanostructures: An n-type TiO₂ layer was deposited on the Sb₂Se₃ nanostructures using an atomic layer deposition (ALD) system (NCD Inc., Daejeon, Korea). ALD precursors, titanium(IV) tetraisopropoxide (TTIP), and H₂O were employed as the Ti and O sources, respectively. TTIP was evaporated at 75 °C and the deposition temperature was 160 °C. One ALD cycle consisted of 3 s of TTIP pulse followed by 10 s of N₂ purging and 2 s of H₂O pulse followed by 10 s of N₂ purging. Four hundred deposition cycles were used to obtain a 20 nm thick layer. After deposition, the Sb₂Se₃ nanostructures modified with TiO₂ were annealed at 200 °C in air to remove the impurities and enhance the interfacial contact.^[7]

PEC Measurements: The PEC properties of the Sb₂Se₃ nanostructure photocathodes were characterized with a three-electrode configuration using a potentiostat (SI 1287, Solartron, Leicester, UK). The Sb₂Se₃ photocathodes were employed as working electrodes, whereas an Ag/AgCl/KCl (saturated) electrode and a Pt wire were used as the reference and counter electrodes, respectively. A copper wire was connected to the back contact of the working electrode with conductive Ag paste, and the unnecessary parts of the electrode were then covered with an insulating resin (HYSOL 9642, Henkel, Düsseldorf, Germany). Before PEC measurements, the sample surface was modified with Pt by PEC deposition. Pt deposition was performed by immersing a prepared electrode in a solution containing 0.1 M Na₂SO₄ (99.9%, Sigma-Aldrich, St. Louis, MO, USA) and 10 × 10⁻⁶ M H₂PtCl₆ (Sigma-Aldrich, St. Louis, MO, USA). The PEC measurement used simulated solar light illumination (AM 1.5 G, Newport Corporation) while the PEC cell was submerged in a 0.1 M aqueous H₂SO₄ solution. Calibration of the one-sun level was performed using a standard Si reference cell certified by the Newport Corporation, consisting of a readout device and a 2 × 2 cm² calibrated solar cell made of monocrystalline silicon. In all cases, the electrodes were front illuminated and the applied potentials were referred to the RHE scale for the sake of comparison with other reports. To convert the potential, the following equation was employed

$$E_{\text{RHE}} = E_{\text{Ag/AgCl}} + 0.059 \text{ pH} + 0.197 \quad (2)$$

IPCE spectra of the Sb₂Se₃ photocathodes were measured under the irradiation of the monochromatic light at 0 V versus RHE (CIMPS-Quantum efficiency/IPCE, Zahner, Germany). The photon flux was determined using a calibrated Si photodiode.

For H₂ detection, all the cell compartments were thoroughly sealed in a quartz tube with a rubber septum to prevent any gas leakage. During irradiation, the headspace gas (150.00 ± 0.01 mL) of the reactor was intermittently sampled using a gastight syringe and analyzed for H₂

using a gas chromatogram (6500GC system, YL Instrument, Anyang, Korea) equipped with a pulsed discharge detector and molecular sieve column.

Supporting Information

Supporting Information is available from the Wiley Online Library or from the author.

Acknowledgements

This work was supported by a National Research Foundation (NRF) of Korea grant funded by the Korean government (Ministry of Science and ICT) (No. 2012R1A3A2026417).

Conflict of Interest

The authors declare no conflict of interest.

Keywords

anisotropy, photoelectrochemical water splitting, Sb₂Se₃ nanostructures, thiol-amine mixture ratio

Received: October 17, 2017

Revised: December 12, 2017

Published online: January 23, 2018

- [1] Y. Tachibana, L. Vayssieres, J. R. Durrant, *Nat. Photonics* **2012**, *6*, 511.
- [2] K. Sivula, R. van de Krol, *Nat. Rev. Mater.* **2016**, *1*, 15010.
- [3] L. Ji, M. D. McDaniel, S. Wang, A. B. Posadas, X. Li, H. Huang, J. C. Lee, A. A. Demkov, A. J. Bard, J. G. Ekerdt, E. T. Yu, *Nat. Nanotechnol.* **2015**, *10*, 84.
- [4] Y. Yu, Z. Zhang, X. Yin, A. Kvit, Q. Liao, Z. Kang, X. Yan, Y. Zhang, X. Wang, *Nat. Energy* **2017**, *2*, 17045.
- [5] O. Khaselev, J. A. Turner, *Science* **1998**, *280*, 425.
- [6] A. Standing, S. Assali, L. Gao, M. A. Verheijen, D. van Dam, Y. Cui, P. H. L. Notten, J. E. M. Haverkort, E. P. A. M. Bakkers, *Nat. Commun.* **2015**, *6*, 7824.
- [7] A. Paracchino, V. Laporte, K. Sivula, M. Grätzel, E. Thimsen, *Nat. Mater.* **2011**, *10*, 456.
- [8] T. W. Kim, K.-S. Choi, *Science* **2014**, *343*, 990.
- [9] W. Yang, Y. Oh, J. Kim, M. J. Jeong, J. H. Park, J. Moon, *ACS Energy Lett.* **2016**, *1*, 1127.
- [10] H. Kumagai, T. Minegishi, N. Sato, T. Yamada, J. Kubota, K. Domen, *J. Mater. Chem. A* **2015**, *3*, 8300.
- [11] H. C. Rojas, S. Bellani, F. Fumagalli, G. Tullii, S. Leonardi, M. T. Mayer, M. Schreier, M. Grätzel, G. Lanzani, F. Di Fonzo, M. R. Antognazza, *Energy Environ. Sci.* **2016**, *9*, 3710.
- [12] K. Zeng, D.-J. Xue, J. Tang, *Semicond. Sci. Technol.* **2016**, *31*, 063001.
- [13] Y. Zhou, M. Leng, Z. Xia, J. Zhong, H. Song, X. Liu, B. Yang, J. Zhang, J. Chen, K. Zhou, J. Han, Y. Cheng, J. Tang, *Adv. Energy Mater.* **2014**, *4*, 1301846.
- [14] R. J. Mehta, C. Karthik, W. Jiang, B. Singh, Y. Shi, R. W. Siegel, T. Borca-Tasciuc, G. Ramanath, *Nano Lett.* **2010**, *10*, 4417.
- [15] Y.-Q. Liu, M. Zhang, F.-X. Wang, G.-B. Pan, *J. Mater. Chem. C* **2014**, *2*, 240.

- [16] J. Yang, Y. Lai, Y. Fan, Y. Jiang, D. Tang, L. Jiang, F. Liu, J. Li, *RSC Adv.* **2015**, *5*, 85592.
- [17] W. Luo, A. Calas, C. Tang, F. Li, L. Zhou, L. Mai, *ACS Appl. Mater. Interfaces* **2016**, *8*, 35219.
- [18] R. R. Prabhakar, W. Septina, S. Siol, T. Moehl, R. W. Joliat, S. D. Tilley, *J. Mater. Chem. A* **2017**, *5*, 23139.
- [19] L. Zhang, Y. Li, C. Li, Q. Chen, Z. Zhen, X. Jiang, M. Zhong, F. Zhang, H. Zhu, *ACS Nano*, **2017**, *11*, 12753.
- [20] J. Kim, W. Yang, Y. Oh, H. Lee, S. Lee, H. Shin, J. Kim, J. Moon, *J. Mater. Chem. A* **2017**, *5*, 2180.
- [21] A. I. Hochbaum, P. Yang, *Chem. Rev.* **2010**, *110*, 527.
- [22] C. Chen, D. C. Bobela, Y. Yang, S. Lu, K. Zeng, C. Ge, B. Yang, L. Gao, Y. Zhao, M. C. Beard, J. Tang, *Front. Optoelectron.* **2017**, *10*, 18.
- [23] Y. Zhou, L. Wang, S. Chen, S. Qin, X. Liu, J. Chen, D.-J. Xue, M. Luo, Y. Cao, Y. Cheng, E. H. Sargent, J. Tang, *Nat. Photonics* **2015**, *9*, 409.
- [24] L. Wang, D.-B. Li, K. Li, C. Chen, H.-X. Deng, L. Gao, Y. Zhao, F. Jiang, L. Li, F. Huang, Y. He, H. Song, G. Niu, J. Tang, *Nat. Energy* **2017**, *2*, 17046.
- [25] G. Chen, J. Zhou, J. Zuo, Q. Yang, *ACS Appl. Mater. Interfaces* **2016**, *8*, 2819.
- [26] Y. Yu, R. H. Wang, Q. Chen, L.-M. Peng, *J. Phys. Chem. B* **2016**, *110*, 13415.
- [27] C. L. McCarthy, R. L. Brutchey, *Chem. Commun.* **2017**, *53*, 4888.
- [28] D. H. Webber, R. L. Brutchey, *J. Am. Chem. Soc.* **2013**, *135*, 15722.
- [29] Q. Tian, G. Wang, W. Zhao, Y. Chen, Y. Yang, L. Huang, D. Pan, *Chem. Mater.* **2014**, *26*, 3098.
- [30] Y. Yang, X. Kang, L. Huang, S. Wei, D. Pan, *J. Power Sources* **2016**, *313*, 15.
- [31] A. Królikowska, A. Kudelski, A. Michota, J. Bukowska, *Surf. Sci.* **2003**, *532*, 227.
- [32] E. L. Elson, J. T. Edsall, *Biochemistry* **1962**, *1*, 1.
- [33] S. Hoshino, H. Hosoya, S. Nagakura, *Can. J. Chem.* **1966**, *44*, 1961.
- [34] D. H. Webber, J. J. Buckley, P. D. Antunez, R. L. Brutchey, *Chem. Sci.* **2014**, *5*, 2498.
- [35] Y. Yang, G. Wang, W. Zhao, Q. Tian, L. Huang, D. Pan, *ACS Appl. Mater. Interfaces* **2014**, *7*, 460.
- [36] H. Liu, J. Zhang, X. Zheng, G. Liu, H. Hu, W. Pan, C. Liu, Q. Hao, H. Chen, *Crystengcomm* **2016**, *18*, 6860.
- [37] Y. Oh, W. Yang, J. Kim, K. Woo, J. Moon, *ACS Appl. Mater. Interfaces* **2015**, *7*, 22570.
- [38] C.-H. Chung, S.-H. Li, B. Lei, W. Yang, W. W. Hou, B. Bob, Y. Yang, *Chem. Mater.* **2011**, *23*, 964.
- [39] B. Yang, D.-J. Xue, M. Leng, J. Zhong, L. Wang, H. Song, Y. Zhou, J. Tang, *Sci. Rep.* **2015**, *5*, 10978.
- [40] M. Hiramatsu, M. Hori, *Carbon Nanowalls: Synthesis and Emerging Applications*, Springer Science & Business Media, New York **2010**.
- [41] J. Ma, Y. Wang, Y. Wang, Q. Chen, J. Lian, W. Zheng, *J. Phys. Chem. C* **2009**, *113*, 13588.
- [42] J. Ma, Y. Wang, Y. Wang, P. Peng, J. Lian, X. Duan, Z. Liu, X. Liu, Q. Chen, T. Kim, G. Yao, W. Zheng, *Crystengcomm* **2011**, *13*, 2369.
- [43] Y. H. Kwon, M. Jeong, H. W. Do, J. Y. Lee, H. K. Cho, *Nanoscale* **2015**, *7*, 12913.
- [44] Y. Liang, Y. Wang, J. Wang, S. Wu, D. Jiang, J. Lian, *RSC Adv.* **2016**, *6*, 11501.
- [45] M. Baia, S. Astilean, T. Llescu, *Raman and SERS Investigations of Pharmaceuticals*, Springer, New York **2008**.
- [46] W. Septina, S. D. Tilley, *Curr. Opin. Electrochem.* **2017**, *2*, 120.
- [47] M. T. Mayer, *Curr. Opin. Electrochem.* **2017**, *2*, 104.
- [48] L. Steier, S. Bellani, H. C. Rojas, L. Pan, M. Laitinen, T. Sajavaara, F. D. Fonzo, M. Gratzel, M. R. Antognazza, M. T. Mayer, *Sustainable Energy Fuels* **2017**, *1*, 1915.
- [49] C. Li, T. Hisatomi, O. Watanabe, M. Nakabayashi, N. Shibata, K. Domen, J.-J. Delaunay, *Energy Environ. Sci.* **2015**, *8*, 1493.
- [50] Z. Chen, H. N. Dinh, E. Miller, *Photoelectrochemical Water Splitting Standard, Experimental Methods, and Protocols*, Springer Briefs in Energy, New York **2013**.
- [51] S. C. Warren, K. Voichovsky, H. Dotan, C. M. Leroy, M. Cornuz, F. Stellacci, C. Herbert, A. Rothschild, M. Gratzel, *Nat. Mater.* **2013**, *12*, 842.
- [52] L. Rovelli, S. D. Tilley, K. Sivula, *ACS Appl. Mater. Interfaces* **2013**, *5*, 8018.
- [53] S. D. Tilley, M. Schreier, J. Azevedo, M. Stefik, M. Graetzel, *Adv. Funct. Mater.* **2014**, *24*, 303.
- [54] S. Hu, C. Xiang, S. Haussener, A. D. Berger, N. S. Lewis, *Energy Environ. Sci.* **2013**, *6*, 2984.
- [55] M. S. Prevot, K. Sivula, *J. Phys. Chem. C* **2013**, *117*, 17879.